Magnetic noise in macroscopic quantum spatial superpositions

Sneha Narasimha Moorthy [1,2] Andrew Geraci [3] Sougato Bose [4] and Anupam Mazumdar [5]
[1]*School of Physical Sciences, National Institute of Science Education and Research, Jatni 752050, India*
[2]*Homi Bhabha National Institute, Training School Complex, Anushaktinagar, Mumbai 400094, India*
[3]*Department of Physics and Astronomy, Northwestern University, 2145 Sheridan Road, Evanston, Illinois, USA*
[4]*Department of Physics and Astronomy, University College London, London WC1E 6BT, United Kingdom*
[5]*Van Swinderen Institute, University of Groningen, 9747 AG Groningen, The Netherlands*

(Received 21 May 2025; accepted 15 July 2025; published 11 August 2025)

In this paper, we show how random fluctuations in the magnetic field gradient jitter the paths of a matter-wave interferometer randomly, hence, decohere the quantum superposition. To create a large spatial superposition with nanoparticles, we envisage embedding a spin in a nanoparticle as a defect and applying an inhomogeneous magnetic field as in a Stern-Gerlach-type experiment to create a macroscopic quantum superposition. Such matter-wave interferometers are the cornerstone for many new fundamental advancements in physics; particularly, adjacent matter-wave interferometers can use entanglement features to test physics beyond the standard model, test the equivalence principle, improve quantum sensors, and test the quantum nature of space-time in a laboratory. In particular, we study how white and flicker noise induces decoherence for a setup involving superconducting wires embedded in a chip. We show that to obtain a tiny spatial superposition of a nanometer separation, $\Delta x \approx O(10^{-9})\,\mathrm{m}$ and to minimize decoherence, $\Gamma \leqslant O(\omega_0/2\pi)$, where Γ is the dephasing rate and ω_0 is the frequency of the oscillator, we will need current fluctuations to be $\delta I/I \leqslant O(10^{-8})$, which is not impossible to obtain in superconducting wire arrangements. For such tiny fluctuations, we demonstrate that the Humpty-Dumpty problem in a matter-wave interferometer arising from a mismatch in position and momentum does not cause a loss in contrast.

DOI: 10.1103/9n6y-cc7r

I. INTRODUCTION

The color-center defects, known as a nitrogen-vacancy (NV) center in a nanodiamond, have a multitude of applications from quantum metrology to quantum sensors [1]. Furthermore, matter-wave interferometers with an NV-centered nanodiamond open up a unique testing ground for fundamental physics, such as testing the quantum nature of space-time. Recently, the authors of Refs. [2–5], see also [6] proposed a protocol to test the quantum nature of space-time in a laboratory via spin entanglement witness [2], see also Refs. [7–14]. Entanglement provides a bona fide quantum correlation, which cannot be mimicked by any classical feature, see Ref. [15]. If two masses in quantum superpositions can be entangled *solely* via gravity, then the space-time ought to behave like a quantum entity [4,5], known as the quantum gravity mediated entanglement of masses (QGEM) protocol. It is well known that entanglement between two quantum systems requires quantum interaction, or quantum mediator, which is the essence of a theorem known as local operations and classical communication (LOCC), which cannot entangle the two quantum systems.

Entanglement-based protocols can be used to witness relativistic corrections to the Coulomb potential [16], post-Newtonian corrections to the low-energy quantum theory of gravity [17], massive graviton in the context of brane-world scenarios [18], modified theories of low-energy quantum gravity [19,20], physics beyond the standard model [21], and tests of the quantum version of the equivalence principle [22]. Most importantly, we can also test the entanglement between matter and photon degrees of freedom [10], which will certify the spin-2 nature of the graviton as a mediator, and will provide a quantum entanglement version of the light-bending experiment due to the quantum-natured graviton. Also, matter-wave interferometers can ideally act as a quantum sensor, detecting external accelerations due to gravity [23–25], electromagnetic interactions [26–30], and high-frequency gravitational waves [31].

Any of these experimental protocols will be subject to decoherence [32] due to many external interactions that are random. In general, any matter-wave interferometer is sensitive to external noise and fluctuations in ambient pressure, temperature, current, voltage, etc. [25,27,33–38]. There is phonon-induced noise [39–41] and fluctuation in the spin degrees of freedom during the dynamics of rotation of the rigid body [42,43], all leading to dephasing and decoherence, see Refs. [32,44,45], and loss of contrast [46–49] In the backdrop of all the above extensive studies of decoherence, however, the most important is arguably the systematic noise stemming from the nature of the protocol itself. As a Stern-Gerlach mechanism is initiated by magnetic-field gradients, these gradients form the core of the systematic noise. How much of such a noise can be tolerated then becomes an important question intrinsic to the process of wave function splitting and recombination.

For NV-centered nanodiamonds, it is possible to create a spin superposition of $|+1\rangle$ and $|-1\rangle$ states, and then by apply-

ing the Stern-Gerlach force on the spin, which is susceptible to the external inhomogeneous magnetic field [49,50], it is possible to separate the center-of-mass motion of the nanodiamond onto left and right trajectories before bringing them together to perform one-loop interferometry, thereby creating a Schrödinger cat state. There are many variants of this scheme, see Refs. [2,31,42,43,51–61]. One might expect that we would be able to cool the initial state of the center-of-mass motion [62–66] before creating the spatial superposition.

In the QGEM protocol, precise control over the external noise sources is crucial to maintain coherence in the spatial superposition states. Since the setup prescribed in Ref. [2] is based on diamagnetic levitation, see Refs. [36,37,67], and to create the superposition, we also rely on the inhomogeneous magnetic field. Hence, any fluctuations in the magnetic field will give rise to random jitter, decoherence. Typically, these random jitters will be the dominant source of dephasing. The fluctuations in the magnetic field originate from the current-carrying wires embedded in the chip, see Ref. [67].

The current analysis focuses on characterizing the dephasing introduced by such noise by modeling using classical stochastic processes at the Lagrangian level. We specifically consider two types of noise: Gaussian white noise and $1/f$ (flicker or pink) noise, and investigate their respective impacts on the phase evolution of the interferometric superposition. We then analyze the Humpty-Dumpty problem in the one-loop matter-wave interferometer, see Refs. [46–49]. The issue is that the fluctuations in the path affect the position and the momentum of both the left and right arms of the interferometer; hence, any classical mismatch will turn into a loss of contrast in the interference pattern. We will consider the constraints on the current fluctuations from the dephasing and show how much the mismatch is in the classical trajectories in the matter-wave interferometer.

II. FLUCTUATIONS AND DEPHASING

Let us consider the following general Lagrangian for an interferometer:

$$L_j = \tfrac{1}{2}mv_j^2 - A_j x_j^2 - B_j x_j - C_j \quad \forall\ j \in R, L, \tag{1}$$

where $j = R, L$ denote the two arms of the interferometer. The coefficients A_j, B_j, and C_j are system-dependent constants in an ideal noiseless scenario. However, in a realistic experimental setup, these parameters acquire time-dependent fluctuations due to noise sources in the system. The ensemble statistics of these fluctuations depend on the nature of the noise present. Here m is the mass of the interferometer, and v_j are the velocities of the two arms. We show how linear in position and quadratic terms appear in the Lagrangian by taking a simple example of Stern-Gerlach-type interferometery [49,50,53,54].

The phase difference between the two paths, $\Delta\phi(t)$ (corresponding to the two interferometer paths), accumulates throughout the experiment.

$$\Delta\phi = \int_{t_i}^{t_f} (L_R - L_L)dt. \tag{2}$$

In the absence of noise, this phase difference purely reflects the differential evolution of the two paths. However, noise in the system introduces additional stochastic contributions $\delta\phi$ to this phase difference, leading to dephasing.

Note that if C_j does not contain any element that introduces fluctuations, it does not affect $\delta\phi$. We shall see that this will be the case in our setup, see below. The equations of motion change randomly if there is an external noise. Let x_j be the trajectory that satisfies the equations of motion (EOM) before the introduction of the noise, and x_j^{tot} be the trajectory that satisfies the EOM after the introduction of noise. Then,

$$\delta x_j = x_j^{\text{tot}} - x_j \tag{3}$$

is the deviation in trajectory due to the introduction of noise. However, in the first analysis, we shall always assume that the two trajectories meet to interfere after the completion of one loop. Later on, we will relax this condition and study the Humpty-Dumpty problem which will lead to the loss of contrast.

At the lowest order, we assume that the fluctuations affect the coefficients A_j, B_j, C_j only and not the trajectories themselves. Hence, we obtain:

$$\delta\phi = \int_{t_i}^{t_f} \big[\big(\delta A_L x_L^2 - \delta A_R x_R^2\big) + (\delta B_L x_L - \delta B_R x_R) + (\delta C_L - \delta C_R)\big]dt. \tag{4}$$

Since noise is a stochastic process, we can only characterize ensemble averages of noise. Hence, we can theoretically calculate the average deviation in phase difference that the noise contributes to. If the experiment lasts for a total time T_{expt}, then any noise with a frequency lower than T_{expt}^{-1} (i.e., time period longer than T_{expt}) would be effectively static over the course of the experiment. This means it would appear as a constant offset rather than as a fluctuating noise. Frequencies just below T_{expt}^{-1} will start to be averaged out, and ones much below are effectively static. In contrast, for noise to have a measurable effect as a fluctuating signal within the experiment, its frequency should be at least comparable to T_{expt}^{-1} or higher. Thus, we set the lower-frequency cutoff as $\omega_{\min} = 2\pi/T_{\text{expt}}$, ensuring that all relevant frequencies contributing to the phase decoherence are considered. To quantify the impact of the noise in the phase evolution, we evaluate the ensemble-averaged variance of the phase difference, denoted Γ, assuming that the noise is Gaussian:

$$\Gamma = \lim_{\tau\to\infty} \frac{1}{\tau} E[(\delta\phi(\tau))^2] \tag{5}$$

$$= \frac{1}{\hbar^2}\int_{\omega_{\min}}^{\infty} S(\omega)|\Sigma_i\sqrt{F_i(\omega)}|^2 d\omega, \tag{6}$$

where τ is the largest time period of the contributing noise,[1] ω is the angular frequency of noise, $S(\omega)$ is the power spectral density (PSD) of the noise, and $F_i(\omega)$ is a system-dependent

[1]The contribution of noise to dephasing can be regularized either by constraining the integration range in frequency space (i.e., imposing a lower bound $\omega_{\min} \sim 2\pi/T_{\text{expt}}$) or by limiting the noise time period $\tau \sim T_{\text{expt}}$. While doing both is mathematically rigorous, constraining either variable is typically sufficient to isolate the relevant spectral behavior of the noise.

response/transfer function that encodes how these fluctuations influence the accumulated phase. Equation (6) is a result of the Weiner-Khinchin Theorem, see Refs. [68,69]. We refer to Appendix A for the derivation of Eq. (6).

The function $F(\omega)$ contains information about how susceptible the system is to noise at a given frequency. In the initial analysis we neglect the effect of the noise on the trajectory itself so that we may assume that at the end of a one-loop interferometer, the paths meet. Then we compute the transfer function by considering the difference in the trajectory between the right and left arms of the interferometer in the frequency domain. They are given by the linear and the quadratic part of the EOM as

$$F_1(\omega) \propto \left| \int_{t_i}^{t_f} dt (x_R - x_L) e^{i\omega t} \right|^2, \tag{7}$$

$$F_2(\omega) \propto \left| \int_{t_i}^{t_f} dt \left(x_R^2 - x_L^2\right) e^{i\omega t} \right|^2. \tag{8}$$

In case the sign of a term in the Lagrangian contributing to the noise is dependent on the spin of the state [e.g., $\delta B_R = -\delta B_L$ in Eq. (1)], then the following transfer functions would contribute as well:

$$F_3(\omega) \propto \left| \int_{t_i}^{t_f} dt (x_R + x_L) e^{i\omega t} \right|^2, \tag{9}$$

$$F_4(\omega) \propto \left| \int_{t_i}^{t_f} dt \left(x_R^2 + x_L^2\right) e^{i\omega t} \right|^2. \tag{10}$$

In Eqs. (8)–(10), we have assumed that δA_L and δB_L are some linear functions in δA_R and δB_R, respectively.

The noise spectrum $S(\omega)$ depends on the statistical properties of the fluctuations or noise. For illustration, we will consider two kinds of noise, one is white noise to get an estimation of how large a dephasing we can tolerate; and the second, flicker noise as superconducting wires are known to exhibit $1/f$ magnetic noise due to surface spin fluctuations and disorder—making it a potentially dominant source of low-frequency decoherence in our setup. This type of noise is very common in magnetic fields generated from superconducting wires, see for a review Refs. [70–72]. We discuss their properties below:

(1) For white noise, $S(\omega) = A^2$ is constant across all frequencies. White noise is characterized by the following statistics:

$$E[\delta\eta(t)] = 0, \tag{11}$$

$$E[\delta\eta(t)\delta\eta(t')] = A^2 \delta(t - t'). \tag{12}$$

From Eq. (12), we obtain the following PSD for white noise:[2]

$$S_{\eta\eta}(\omega) = \lim_{\tau\to\infty} \frac{1}{\tau} E[\delta\tilde{\eta}_\tau(\omega)\delta\tilde{\eta}_\tau^*(\omega)] = A^2. \tag{13}$$

Here, A is a constant that depends on the characteristics of the noise source. In Sec. IV, we constrain A based on the maximum tolerable dephasing in the simplest matter-wave interferometer.

(2) For flicker noise, $S(\omega) \propto 1/|\omega|^\alpha$, which leads to stronger low-frequency contributions, where $\alpha \in [0.5, 1.5]$,[3] see Refs. [73,74]. The magnetic field is considered to be produced by current flowing in a conductor or a superconducting wire. Any noise in the current will cause a noise in the magnetic-field gradient. We consider the flicker noise contribution with the following PSD [73,74]:

$$S_{II}(\omega) = \lim_{\tau\to\infty} \int_{-\frac{\tau}{2}}^{\frac{\tau}{2}} E[I(t)I(t')] e^{i\omega(t-t')} dt dt'$$

$$= E[\tilde{I}(\omega)\tilde{I}^*(\omega)] = \frac{KI^2}{|\omega|^\alpha}, \tag{14}$$

where I is the DC current without fluctuations and K is a source-dependent constant.[4] $\alpha \approx 1$[5] in the case of superconducting wires made of Nb.

Since we are levitating the nanoparticle at a distance d away from a current-carrying chip, see Ref. [67], we consider the thin-wire limit and that the wire is much longer than the nanoparticle such that we can take the infinite-wire limit in our computations:[6]

$$B = \frac{\mu_0 I}{2\pi d}. \tag{15}$$

The magnetic field gradient is given by

$$\eta_0 = \frac{\partial B}{\partial x} = -\frac{\mu_0 I}{2\pi d^2}. \tag{16}$$

Hence, the PSD of the noise due to the gradient of the magnetic field is given by [73,74]

$$S_{\eta\eta}(\omega) = \frac{\mu_0 S_{II}}{2\pi d^2} = \frac{\mu_0 K I^2}{2\pi d^2 |\omega|^\alpha}. \tag{17}$$

By analyzing the dependence of Γ on the noise spectral density, we aim to quantify the impact of the two types of magnetic-field fluctuations on the coherence of spin superpositions in a Stern–Gerlach-type interferometer [49,50,53,54]. In particular, we consider the parameter regime relevant to the experimental proposal of levitating the nanodiamond, see Ref. [67], and derive constraints on the associated experimental parameters.

[2] $\delta\tilde{\eta}_\tau(\omega) = \frac{1}{2\pi}\int_{-\tau}^{\tau} \delta\eta(t)\, e^{i\omega t}\, dt$.

[3] $\alpha = 0$ gives back white noise statistics. $\alpha = 2$ gives back Brownian noise statistics.

[4] The universal flux noise for SQUIDS and superconducting thin films is given by $S_\Phi = A/f^\alpha$ with amagnitude of $A \sim 5$–$10\ \mu\Phi_0/\sqrt{\text{Hz}}$ at 1 Hz, and $0.58 < \alpha < 0.80$ [70], where $S_\Phi = S_{\eta\eta}/(A^2L^2)$, and L and A are the length and area of the superconductor.

[5] For elements, Al: $\alpha \in [1, 1.1]$ and Nb: $\alpha \in [1, 1.4]$ [74].

[6] The current in Eq. (15) is an effective current from a combination of wires, which is responsible for creating the superposition. Note that current-carrying wires on the chip are also required to levitate the nanodiamond, see Refs. [67] and [75]. However, here we are interested in the wire configuration which will trigger the linear magnetic field gradient along one spatial dimension to create a superposition, see Refs. [53,54,76].

III. NV-CENTERED NANODIAMOND

For illustration, consider an NV-centered nanoparticle with a mass m in a spin superposition entering a Stern-Gerlach-type interferometer at $t = 0$. The following is the Lagrangian for each of the states composing the superposition [53–55]:[7]

$$L_j = \frac{1}{2}mv_j^2 - \frac{1}{2}m\omega_0^2 x_j^2 - \left(S_{xj}\hbar\gamma_e\eta_0 - \frac{\chi_\rho m}{\mu_0}B_0\eta_0\right)x_j + \frac{\chi_\rho m}{2\mu_0}B_0^2 - S_{xj}\hbar\gamma_e B_0 - \hbar D S_z^2 \quad \forall\ j \in R, L, \tag{18}$$

where the external magnetic field is taken to be $\mathbf{B} = (B_0 + \eta_0 x)\hat{x}$,[8] and $\chi_\rho = -6.286 \times 10^{-9}\ \mathrm{m^3\,kg^{-1}}$ (for the nanodiamond) represents the mass magnetic susceptibility of the particle. We consider dynamics only along the x axis. S_{xj} is the spin of the particle in state j. R, L represent the two spins (in the x basis) and spatial superposition states ($S_{xR} = 1$ and $S_{xL} = -1$); they denote the two arms of the interferometer. Note that the spin and the center of mass are entangled in an SG interferometer. D in the last term refers to the zero-field splitting, which in the case of NV centers is $D = 2.87$ GHz [77] and is a constant and ω_0 is defined as follows, see Refs. [53,54]:

$$\omega_0 = \left(-\frac{\chi_\rho}{\mu_0}\right)^{1/2}\eta_0. \tag{19}$$

From Eq. (18), we obtain the following equation of motion:

$$m\ddot{x}_j(t) = -m\omega_0^2 x_j(t) - C_j\eta_0, \tag{20}$$

where

$$C_j = \left(S_{xj}\hbar\gamma_e - \frac{\chi_\rho m}{\mu_0}B_0\right). \tag{21}$$

Imposing $x_j(0) = 0$ and $\dot{x} = 0$, we get

$$x_j(t) = \frac{C_j\eta_0}{m\omega_0^2}[\cos(\omega_0 t) - 1]. \tag{22}$$

Now, we wish to probe the effect of noise in the magnetic field in this setup. Hence, we consider the magnetic field to have a time-dependent component arising from the noise. Thus consider, along the x direction,

$$B(t) = B_0 + [\eta_0 + \delta\eta_0(t)]x. \tag{23}$$

where $\delta\eta_0(t)$ represents the noise in the magnetic field gradient.[9] The noise is characterized by the ensemble average over time of its various time correlation functions: $E[\delta\eta(t)]$, $E[\delta\eta(t)\delta\eta(t')]$, see Ref. [78]. We shall focus on two types of noise: white noise and flicker noise.

In a closed-loop interferometric experiment involving a spin superposition, the spin readout is typically performed after the interferometric path is closed to extract information about the evolution of the constituent spin states during the experiment. Our objective is to study how noise influences the relative phase accumulation between these spin components. In addition to phase fluctuations, noise also perturbs the spatial trajectory of the particle, which we denote by δx_j. Thus, the effect of noise relevant to us is encoded in the difference in the phases between the spin states arising due to the noise:

$$\delta\phi = \frac{1}{\hbar}\int_0^T [L_R(t) - L_L(t)]dt \tag{24}$$

$$= \frac{1}{\hbar}\int_0^T \Bigg[-\frac{1}{2}m\left(-\frac{\chi_\rho}{\mu_0}\right)2\eta_0\delta\eta(t)\left(x_R^2 - x_L^2\right) - \frac{1}{2}m\left(-\frac{\chi_\rho}{\mu_0}\right)\eta_0^2(2x_R\delta x_R - 2x_L\delta x_L) - \hbar\gamma_e\delta\eta(t)(x_R + x_L) - \hbar\gamma_e\eta_0(\delta x_R + \delta x_L) + \frac{\chi_\rho m}{\mu_0}B_0\delta\eta(t)(x_R - x_L) + \frac{\chi_\rho m}{\mu_0}B_0\eta_0(\delta x_R - \delta x_L)\Bigg]dt, \tag{25}$$

where $L_j(t)$ denotes only the time-dependent parts of L_j.[10]

We have ignored terms with higher-order dependence on deviations due to noise—higher order in $\delta\eta$ and δx_j. In the present analysis, we shall ignore the contribution of the fluctuations in the trajectory; the latter is considered in Appendix D. In effect, we will be considering

$$\delta\phi = \frac{1}{\hbar}\int_0^T \Bigg[-\frac{1}{2}m\left(-\frac{\chi_\rho}{\mu_0}\right)2\eta_0\delta\eta(t)\left(x_R^2 - x_L^2\right) - \hbar\gamma_e\delta\eta(t)(x_R + x_L) + \frac{\chi_\rho m}{\mu_0}B_0\delta\eta(t)(x_R - x_L)\Bigg]dt. \tag{26}$$

We now Fourier transform to the frequency domain, substitute the trajectory using Eq. (22) and simplify further:

$$\delta\phi = H\left(\int_{-\infty}^{-\omega_{\min}} + \int_{\omega_{\min}}^{\infty}\right)\Bigg[\delta\tilde{\eta}(\omega)\int_0^T \times \left\{\frac{(\cos(\omega_0 t) - 1)\cos(\omega_0 t)}{\omega_0^2}\right\}e^{i\omega t}dt\Bigg]d\omega, \tag{27}$$

[7]We are assuming that the nanoparticle is levitated via diamagnetic levitation. We are ignoring the effects of gravity or any fluctuations due to gravity. Such fluctuations to some extent were discussed in our earlier papers, see Refs. [23,25].

[8]We assume that the magnetic field is in the x-y plane, therefore, $B_y = -\eta_0 y\hat{y}$. However, we are assuming that the superposition will take place in one dimension. We are assuming an ideal case where we take the initial condition of $y = 0$. In reality, it will be extremely hard, and this will require knowing the center-of-mass motion along the x, z directions extremely well. We will need to initiate the experiment at $y = 0$, in which case there will be no displacement due to the external inhomogeneous magnetic field along this direction.

[9]We do not include the fluctuations in the magnetic field since we focus on the noise due to the source creating the magnetic field gradient—a wire-like approximation for the current source. However, the same procedure can be extended to include the noise in the bias field, say, due to a Helmholtz-coil current source.

[10]Had we included fluctuations in the bias field, we would have an additional term like $(S_{xR} - S_{xL})\hbar\gamma_e\delta B_0$.

where

$$H = \frac{1}{\hbar}\left(4\hbar\gamma_e B_0 \eta_0 \frac{\chi_\rho}{\mu_0}\right) = 4\gamma_e B_0 \eta_0 \frac{\chi_\rho}{\mu_0}. \tag{28}$$

In this process of simplification from Eq. (26) to Eq. (27), it was noticed that the effect of magnetic field perturbations on the interaction of the spin with the external magnetic field gradient and that of the diamagnetic environment with the external magnetic field gradient are equal, i.e., the second and third terms in Eq. (26) are equal upon substituting for x_j with Eq. (22).

In the following analysis, we compute Γ, as defined in Eq. (6), for both white and flicker noise spectra in a simple Stern–Gerlach-type interferometer. Based on the resulting dephasing, we then place constraints on the parameters characterizing the noise source.

IV. NOISE IN BASIC ONE-LOOP INTERFEROMETER

In this section, we will be computing the values of dephasing under different noise statistics. We wish to see what should be the maximum values of A^2 in the case of white noise [Eq. (12)] and K in the case of flicker noise [Eq. (17)] so that the coherence at the end of the interferometer due to these noises is around 10%. We also study the trend of the dephasing rate under various experimental parameters, and hence we can extrapolate to other values of coherence. Since we want an order-of-magnitude estimate, we carry out a simple first analysis for a single-loop interferometer and do not consider time-dependent spin states (as would be the case in the QGEM protocol). That is, we just consider a simple harmonic oscillator case given by Eq. (18).

Using Eq. (27), we obtain the dephasing for a general noise PSD to be

$$\Gamma = \frac{8H^2}{\omega_0^5}\int_{\omega_{\min}/\omega_0=1}^{\infty} S_{\eta\eta}(\xi) F_{\rm HO}(\xi) d\xi, \tag{29}$$

where we consider general noise statistics according to Eq. (13), and $\xi = \omega/\omega_0$, and $F_{\rm HO}(x)$ is given by

$$\begin{aligned} F_{\rm HO}(\xi) &= \sin^2(\pi\xi)\left[\frac{1}{2\xi} + \frac{\xi}{2(\xi^2-4)} - \frac{\xi}{\xi^2-1}\right]^2 \\ &= \frac{1-\cos(2\pi\xi)}{2}\left[\frac{\xi^2+2}{\xi(\xi^2-4)(\xi^2-1)}\right]^2. \end{aligned} \tag{30}$$

We can consider Eq. (30) to represent the effective transfer function[11] for a harmonic oscillator up to a system constant (and under the assumption of ignoring deviations in the trajectory). Note that the transfer function is an even function in ξ, and hence the integral over negative frequencies is the same as that of positive values. Next, we shall compute the integral over ω using numerical methods, for various forms of $S(\omega)$.

[11]It would be more meaningful to consider $4H^2/\omega_0^5 F_{\rm HO}$ to be the effective transfer function because it captures the system-dependent parameters via H and ω_0.

TABLE I. List of parameters used in the calculation.

Parameter	Value
Electron gyromagnetic ratio γ_e	$1.761 \times 10^{11}\ \mathrm{s^{-1}\,T^{-1}}$
Bias magnetic field B_0	0.2 T
Current I	12 A
Distance d from wire	20 μm
Nanodiamond density ρ	$3.5 \times 10^3\ \mathrm{kg\,m^{-3}}$
Mass magnetic susceptibility χ_ρ	$-6.286 \times 10^{-9}\ \mathrm{m^3\,kg^{-1}}$

We first compute the parameter values expected in a typical experiment, so that we can find the bounds on the order of magnitude of noise. These parameters are motivated by the experimental setup of levitating nanoparticles in a diamagnetic trap, see Ref. [67].

A. Estimation of parameters

The values of parameters considered in our analysis are presented in Table I. The values of the current and the distance from the wire are motivated from Ref. [67]. Next, we derive the key quantities η_0, H [see Eq. (28)], ω_0, and the maximum spin state separation $\Delta x_{\max}$ using the parameter values from Table I. We can evaluate the magnetic field gradient using Eq. (16):

$$\eta_0 = -\frac{\mu_0 I}{2\pi d^2} = -0.6 \times 10^4\ \mathrm{T\,m^{-1}}. \tag{31}$$

We can compute H using Eq. (28),

$$H = 4\gamma_e B_0 \eta_0 \frac{\chi_\rho}{\mu_0} = 4.23 \times 10^{12}\ \mathrm{s^{-1}\,m\,kg^{-1}\,A^{-2}}, \tag{32}$$

and ω_0 using Eq. (19),

$$\omega_0 = \left|\left(-\frac{\chi_\rho}{\mu_0}\right)^{\frac{1}{2}}\eta_0\right| = 4.24 \times 10^2\ \mathrm{Hz}. \tag{33}$$

Thus, the experimental time, that is the time taken to complete the one-loop interferometer, is given by

$$T_{\rm expt} = \frac{2\pi}{\omega_0} = 1.48 \times 10^{-2}\ \mathrm{s}. \tag{34}$$

Hence, the coherence is measured by $e^{-\Gamma T_{\rm expt}}$. Thus, for a coherence of 10%, we get

$$\Gamma \approx 155\ \mathrm{Hz^{-1}}. \tag{35}$$

The maximum separation of the spin states occurs at half the time period of the oscillation($t = \pi/\omega_0$) and is found from Eq. (22). The final simplified form of the maximum separation of spin states is given by

$$\begin{aligned} \Delta x|_{\rm Max} &= |x_R(t) - x_L(t)|_{t=\frac{\pi}{\omega_0}} \\ &= \left|\frac{4\hbar\gamma_e\eta_0}{m\omega_0^2}\right| \approx 2.5 \times 10^{-9}\ \mathrm{m}. \end{aligned} \tag{36}$$

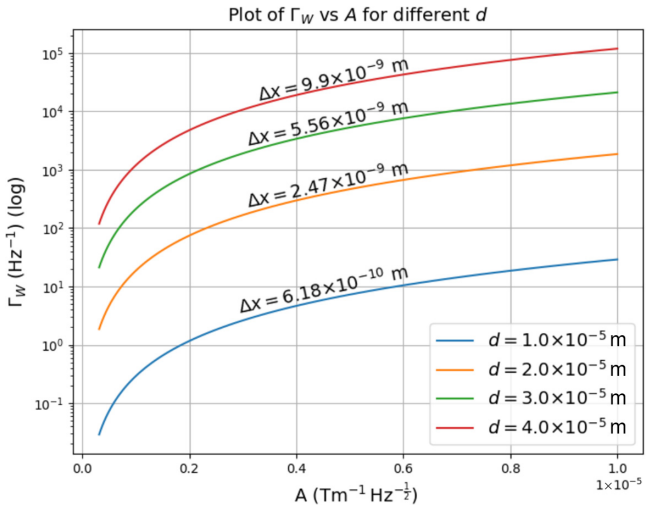

FIG. 1. Dependence of the dephasing rate Γ_W, induced by white noise in the current generating the magnetic field gradient, on the noise amplitude A, for various distances d between the NV diamond and the wire. The current and the values of d are motivated from a levitating nanodiamond diamagnetically, via chip configuration, see Ref. [67]. The remaining parameters follow the simplified Stern-Gerlach model for creating spatial superposition (see Sec. IV A). The quantity Δx, defined in Eq. (36), represents the maximum spatial separation between the spin components of the superposition state. The plot illustrates how both the magnitude of current fluctuations and the spatial configuration significantly affect spin coherence in a Stern-Gerlach-type interferometer. We have ensured here that $\Gamma_W T_{\text{expt}} \leqslant 2.5$ for d $= 20$ μm.

B. White noise

We carry out the ω integrals in Eq. (29) using numerical integration with the PSD for white noise Eq. (12):

$$S_{\eta\eta}(\xi) = A^2. \tag{37}$$

The numerical analysis reveals that, despite the frequency-independent nature of the power spectral density (PSD), the effective transfer function (30) ensures that the resulting dephasing remains finite for a given value of A. A plot of the transfer function is provided in Appendix E. This behavior indicates that the harmonic oscillator is more sensitive to low-frequency noise components than to high-frequency ones.

The following calculation is helpful for any harmonic oscillator potential. We take $T_{\text{expt}} = 2\pi/\omega_0$ since we are considering a single-loop interferometer.[12] Now we impose the bounds on ω: the frequency of the noise has to be greater than the inverse of the total time of the experiment (as discussed before). Thus, we take $\omega_{\text{min}} = \omega_0$. From Eq. (29), we carry out the integration numerically and obtain[13]

$$\Gamma_W = \frac{8H^2}{\omega_0^5} A^2 \int_1^\infty F_{\text{HO}}(\xi)\, d\xi$$

$$\Rightarrow \Gamma_W \approx \frac{8H^2}{\omega_0^5} A^2 \times 1.8\ \text{s}^{-1}, \tag{38}$$

where $H = 4\gamma_e B_0 \eta_0 \frac{\chi_\rho}{\mu_0}$, as defined in Eq. (28). We observe from Fig. 1 that increasing the distance d between the NV-diamond and the wire leads to a decrease in dephasing Γ_W for a given noise amplitude A. Physically, this can be attributed to the reduction in the magnetic field gradient with increasing distance from the wire. Interestingly, a stronger magnetic field gradient leads to a smaller spatial separation Δx between the spin states. This counterintuitive behavior arises because the effective harmonic oscillator frequency ω_0 increases with the field gradient, thereby increasing the confining potential and reducing the spatial spread of the wavepacket.

This introduces a design trade-off: while a smaller magnetic field gradient increases susceptibility to current noise, it also results in a larger superposition size, which enhances the interferometric signal. Also, other noise sources like the electromagnetic field noise [27,79,80] contribute nearer to the current-carrying wire. Hence, we have to choose an optimal magnetic field gradient such that the noise is low but the superposition size gives us measurable effects.

From Eq. (38), we find that, for a tolerable dephasing rate of $\Gamma_W = \Gamma_{W_{\text{max}}}$Hz, A can be constrained using

$$A \lesssim \sqrt{\Gamma_{W_{\text{max}}} \frac{\omega_0^5}{8H^2 \times 1.8}}. \tag{39}$$

Specifically, if we demand that the dephasing rate should be less than ≈100 Hz (i.e, $\Gamma_{W_{\text{max}}} \approx 100$ Hz) and using the values of H and ω_0 from Eqs. (32) and (33), respectively, the noise amplitude is constrained as

$$A \lesssim 2.9 \times 10^{-6}\ \text{T m}^{-1}\ \text{Hz}^{-1/2}. \tag{40}$$

This allows us to estimate the maximum permissible ratio of current noise[14] to signal current for a dephasing rate of $\approx 10^2$ Hz using Eq. (16):

$$\frac{\delta I}{I} \approx \frac{A\sqrt{1.8\,\omega_0}}{\eta_0} = 1.3 \times 10^{-8}. \tag{41}$$

In the above we have taken the configuration where $|\eta_0| \approx 6 \times 10^3\ \text{Tm}^{-1}$.

If we consider noise sensitivity for the total experimental time (say $10^4 \times \frac{2\pi}{\omega_0}$), then the bound on A must be reevaluated

[12] However, to obtain the phase information, we have to carry out about 10^4 to 10^6 experimental runs. Hence, the precision of the measurement increases with the number of experimental runs. However, this also increases the sensitivity to noise. Hence we need to consider $T_{\text{expt}} = 10^4 \times \frac{2\pi}{\omega_0}$ if we consider 10^4 experimental runs. This increases the bandwidth of frequencies to which the experiment is sensitive since $\omega_{\text{min}} = 2\pi/T_{\text{expt}}$.

[13] Since the integrand in Eq. (38) is well defined for all frequencies (refer to Appendix E), we can obtain the upper bound on dephasing by considering $\omega_{\text{min}} = 0$. This gives us $\int_0^\infty F_{\text{HO}}(\xi)d\xi \approx 4.3$ and the upper bound on dephasing is $\Gamma_W \approx \frac{8H^2}{\omega_0^5} A^2 \times 4.3$.

[14] The noise magnitude is given by $[\int_{\omega_0}^\infty S(\omega) F_{\text{HO}}(\omega)\, d\omega]^{1/2}$. This can be intuitively understood as the square root of power, where power is the product of the power spectral density (PSD) and the effective bandwidth.

accordingly. Under this consideration, the frequency bandwidth to which the experiment is sensitive to increases (see footnote 12), for example, corresponding to $T_{\text{expt}} = 10^4 \times \frac{2\pi}{\omega_0}$, $\omega_{\text{min}} = 10^{-4} \times \omega_0$. This further varies the bounds of the integral (see footnote 13) in Eq. (38). Hence Eq. (39) would change accordingly. The bound on A becomes stricter, such as for $T_{\text{expt}} = 10^4 \times \frac{2\pi}{\omega_0}$, $A \lesssim 1.8 \times 10^{-6}\,\text{T m}^{-1}\,\text{Hz}^{-1/2}$. The increase in bandwidth and stricter conditions on A compensate for each other returning the same tolerance for current fluctuations. This is further explained by Eq. (47).

As discussed earlier in this section, the convergence of Γ_W for flat (white) noise spectra arises due to the frequency-dependent suppression built into the harmonic oscillator's transfer function. This indicates that the harmonic oscillator is particularly sensitive to low-frequency noise. Since current noise in conductors typically exhibits a $1/f$ (flicker) behavior, we now turn to an analysis of flicker noise in the next section.

C. Flicker noise

In the case of flicker noise, the PSD in terms of the dimensionless quantity ξ is given by [73,74]

$$S_{\eta\eta}(\xi) = \frac{\mu_0}{2\pi d^2}\frac{KI^2}{|\omega_0|^\alpha |\xi|^\alpha} \equiv \frac{\tilde{K}^2(\omega_0)}{|\xi|^\alpha}, \tag{42}$$

where $\tilde{K} = (\frac{\mu_0}{2\pi d^2}\frac{KI^2}{|\omega_0|^\alpha})^{1/2}$. We once again take $T_{\text{expt}} = 2\pi/\omega_0$ since we are considering a single loop interferometer and we numerically carry out the ω integral. From Eq. (29), we obtain[15]

$$\Gamma_F = \frac{8H^2}{\omega_0^5}\tilde{K}^2(\omega_0)\int_1^\infty \frac{F_{\text{HO}}(\xi)}{|\xi|}d\xi$$
$$\Rightarrow \Gamma_F \approx \frac{8H^2}{\omega_0^5}\tilde{K}^2(\omega_0) \times 1.3\ \text{s}^{-1}. \tag{43}$$

From Fig. 2, we observe that the greater the values of K, the higher the dephasing, as expected. As the spectral exponent α increases, the contribution of high-frequency components in the noise spectrum diminishes, making the noise increasingly dominated by slow, quasistatic fluctuations. These low-frequency drifts behave effectively as static offsets in system parameters over the experimental timescale (as discussed in Sec. II). Consequently, their impact on the system's coherence is reduced, since such slowly varying fluctuations can often be compensated for or averaged out. For this reason, their contribution to dephasing is neglected in this analysis. For superconductors, $\alpha \approx 1$, and for this value of the spectral exponent, we observe the trend of the dephasing rate as a function of source-dependent K. From Fig. 3, we observe that dephasing increases with increasing distance d from the wire. Specifically, doubling d results in an approximate two-order-of-magnitude increase in the dephasing rate Γ_F. This trend arises because the magnetic field gradient generated by the current decreases with distance from the wire. A weaker magnetic field gradient leads to a reduced harmonic confinement frequency. Since the amplitude of flicker noise is inversely proportional to the harmonic frequency, a lower frequency results in increased noise. Physically, a reduced harmonic frequency corresponds to weaker confinement, allowing a larger spatial separation Δx between the spin components of the superposition state. This enhanced separation increases the system's sensitivity to magnetic-field-gradient fluctuations.

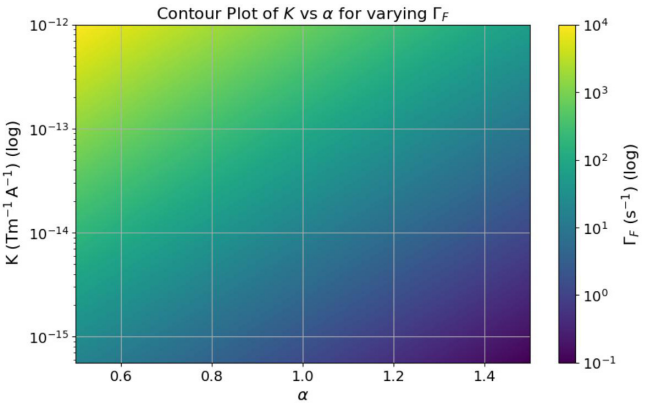

FIG. 2. Contour plot showing the behavior of the source-dependent component of the flicker noise, K as a function of the dimensionless parameter $\alpha \in [0.5, 1.5]$ that determines the dependence of noise statistics on frequency, with the contours representing varying levels of the resulting dephasing rate Γ_F. ω_0, is the characteristic frequency of the system, defined in Eq. (33). Smaller α causes stronger dephasing for the same value of K. This shows that the system is particularly sensitive to low-frequency noise, which is a characteristic trait of flicker noise. The plot helps visualize how different combinations of K and α contribute to decoherence in the system, and it can be used to identify safe operating regions where dephasing remains within acceptable bounds.

From Eq. (43), we find that for a tolerable dephasing rate of $\Gamma_F = \Gamma_{F_{\text{max}}}\text{Hz}$, $\tilde{K}$ can be constrained using

$$\tilde{K} \lesssim \sqrt{\Gamma_{F_{\text{max}}}\frac{\omega_0^5}{8H^2 \times 1.3}}. \tag{44}$$

Specifically, if we demand that the dephasing rate should be less than ≈100 Hz (i.e., $\Gamma_{F_{\text{max}}} \approx 100$ Hz) and using the values of H and ω_0 from Eqs. (32) and (33), respectively, and further using the relation between K and $\tilde{K}$ from Eq. (42), we can constrain K:

$$K \lesssim 0.7 \times 10^{-13}\,\text{T m}^{-1}\,\text{A}^{-1}. \tag{45}$$

[15]The integrand in Eq. (43) is not well defined at $\xi = 0$ (refer to Appendix E), hence to obtain the upper bound on dephasing we need to consider a large but finite number of experimental runs. If we consider 10^4 experimental runs, the total experimental time is given by $T_{\text{expt}} = 10^4 \times \frac{2\pi}{\omega_0}$. Thus $\frac{\omega_{\text{min}}}{\omega_0} = 10^{-4}$. This gives us $\int_{10^{-4}}^{\infty} F_{\text{HO}}(\xi)d\xi \approx 24$ and the corresponding dephasing is $\Gamma_F \approx \frac{8H^2}{\omega_0^5}\tilde{K}^2 \times 24$. Similarly, if we consider 10^6 experimental runs, the dephasing is $\Gamma_F \approx \frac{8H^2}{\omega_0^5}\tilde{K}^2 \times 35.5$. Therefore, the increase in the magnitude of dephasing is utmost of order 10^1.

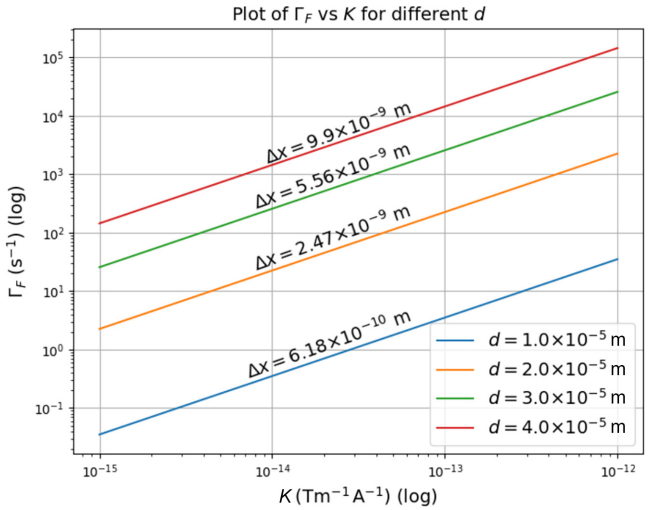

FIG. 3. Dependence of the dephasing rate Γ_F, induced by flicker ($1/f$) noise in the current generating the magnetic field gradient, on the source-dependent noise amplitude K, for various distances d between the NV diamond and the wire. We have fixed $\alpha = 1$ since this is the approximate value of the exponent in the case of superconductors. The parameter K depends on the material properties of the superconducting wire, such as temperature, composition, and fabrication details. All other parameters are fixed as specified in Sec. IV A, consistent with the simplified Stern-Gerlach model. The quantity Δx denotes the maximum spatial separation between the spin components of the superposition state, as defined in Eq. (36). This figure illustrates the sensitivity of spin coherence to both current-noise magnitude and the geometric configuration of the Stern-Gerlach-type interferometer.

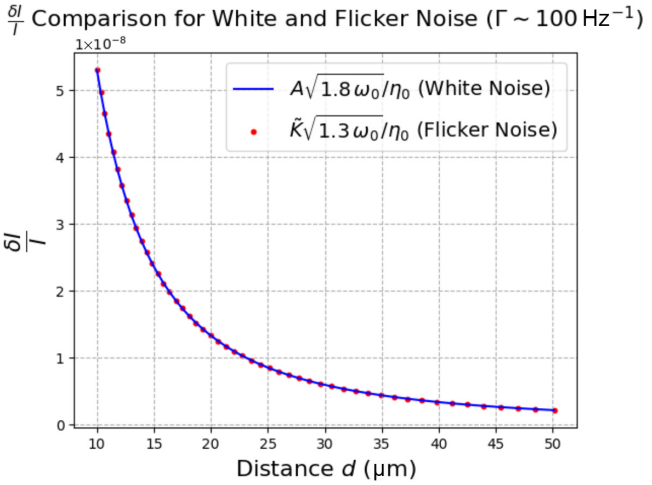

FIG. 4. Comparison of the upper bound on the relative current noise $\delta I/I$ as a function of the particle's distance d from a current-carrying superconductor for a dephasing rate of $\Gamma \approx 10^2$ Hz. The plot includes results for white noise (blue curve) and flicker noise (red dots). As the distance of the particle from the wire increases, the tolerance for noise drops sharply. Despite differing spectra, both noise types impose similar constraints on current fluctuations over the entire distance range, indicating comparable impacts on coherence in this regime.

K is a source-dependent constant; we note that values of similar magnitude have been reported for niobium (Nb) superconductors in previous studies [81].[16]

From this, we can estimate the tolerable ratio of the noise (see footnote 14) and signal amplitudes for the magnetic field gradient and also obtain it in terms of current amplitudes from Eq. (16) at $\omega_0 = 424$ Hz:

$$\frac{\delta I}{I} \approx \frac{\tilde{K}\sqrt{1.3\,\omega_0}}{\eta_0} = 1.3 \times 10^{-8}, \tag{46}$$

where $\tilde{K}$ is defined in Eq. (42).

If we consider noise sensitivity for the total experimental time (say $10^4 \times \frac{2\pi}{\omega_0}$), then the bound on K must be reevaluated accordingly. Under this consideration, the frequency bandwidth to which the experiment is sensitive to increases (see footnote 12), for example, corresponding to $T_{\text{expt}} = 10^4 \times \frac{2\pi}{\omega_0}$, $\omega_{\text{min}} = 10^{-4} \times \omega_0$. This further varies the bounds of the integral[15] in Eq. (43). Hence Eq. (44) would change accordingly. The bound on K becomes stricter, such as for $T_{\text{expt}} = 10^4 \times \frac{2\pi}{\omega_0}$, $K \lesssim 0.04 \times 10^{-13}\,\mathrm{T\,m^{-1}\,A^{-1}}$. The increase in bandwidth and stricter conditions on K compensate for each other returning the same tolerance for current fluctuations. This is further explained by Eq. (47).

D. Comparison

In Fig. 4, we compare the upper bound on the noise-to-signal ratio of the current source ($\delta I/I$) required to maintain a dephasing rate of $\approx 10^2$ Hz for the two types of noise considered in this study: flicker noise and white noise. We find that the bounds on $\delta I/I$ are nearly identical in both cases. While the dephasing rate associated with white noise is inherently larger than that of flicker noise, both noise types exhibit comparable tolerance to current fluctuations.

This observation suggests a potentially broader implication: for any spectral exponent $\alpha \in [0, 1.5]$, the constraints imposed on experimental parameters by dephasing considerations remain approximately constant. Therefore, the requirement on the magnitude of current fluctuations to achieve a given dephasing rate $\approx 10^2$ Hz appears to be relatively robust across different noise spectra. This is because current and magnetic-field-gradient fluctuations are directly related by Eq. (16) and, hence, putting a bound on the dephasing rate obtained from magnetic-field-gradient fluctuations directly yields the bounds on both magnetic field gradient and current fluctuations from Eqs. (38) and (43). Hence, by the definition of noise amplitude (see footnote 14) and

[16]Specifically, Ref. [81] defines a related source-dependent parameter C, which can be related to K in our paper as $C = K\mathcal{A}/T^2$, where $\mathcal{A}$ is the cross-sectional area of the superconducting wire and T is the temperature. In our source, $\mathcal{A} \approx 7.85 \times 10^{-11}$ m^2 and $T \approx 4.2$ K. Thus, we estimate $C \approx 0.3 \times 10^{-23}$ m^2 K^{-2} in our case. This value is one order of magnitude smaller than the reported value of $C = 3.9 \pm 0.4 \times 10^{-23}$ m^2 K^{-2} in 2004. However, given advances in fabrication and noise mitigation, the current state of the art may exhibit lower values of C, and our estimate could be within achievable limits.

from Eq. (29),

$$\frac{\delta I}{I} = \frac{\delta\eta}{\eta_0} = \sqrt{\frac{\Gamma}{2}}\frac{\omega_0^3}{2H\eta_0}. \tag{47}$$

Thus, given an upper bound on the dephasing, the tolerance of current fluctuations is determined by system parameters and not by noise parameters nor the experimental time; i.e., even if we take the total experimental time including all experimental runs ($\approx 10^4 \times \frac{2\pi}{\omega_0}$), it imposes constraints only on the noise parameters like A in the case of white noise and $\tilde{K}$ in the case of flicker noise, but not on the bound of $\delta I/I$.

We also observe that as the distance between the particle and the wire increases, the constraint on the noise-to-signal ratio becomes more stringent in order to maintain low dephasing. This is due to the reduction in the magnetic field gradient η at larger distances, which leads to weaker confinement of the particle, see Ref. [67]. As a result, the system becomes more susceptible to noise-induced fluctuations, thereby requiring a lower noise-to-signal ratio to preserve coherence.

V. HUMPTY-DUMPTY PROBLEM

In Sec. II, we discussed the general form of noise analysis in cases where the deviations in the trajectory due to the noise are ignored. Now we shall analyze the impact of the deviations in the trajectory [indicated by δx_j in Eq. (25)] due to fluctuations in the magnetic field gradient and quantify this effect with the contrast of the interference. The contrast $\mathcal{C}$ in an interferometer experiment lies in the range [0,1], where $\mathcal{C} = 1$ means that the interferometer closes and $\mathcal{C} = 0$ means that the interferometer does not close and hence spin-readout is not possible, see the definition below. The latter is part of the Humpty-Dumpty problem of irreversibility associated with quantum measurement, specifically the practical impossibility of restoring a coherent superposition once decoherence has occurred. We analyze the value of $\mathcal{C}$ subject to the parameters obtained above, see Refs. [46–49]. In Appendix E, we derive the dephasing when the deviations in the trajectory are accounted for in Eq. (25).

A. Equations of motion

We start by analyzing the equation of motion of the deviations from the trajectory δx_j. They satisfy the following equation [obtained from Eqs. (3), (18), and (20)]:

$$\delta\ddot{x}_j(t) + \omega_0^2\delta x_j(t) = -\frac{C_j\delta\eta(t)}{m}[2\cos(\omega_0 t) - 1]. \tag{48}$$

To solve this, we obtain

$$\delta x_j(t) = -\frac{C_j}{m\omega_0}\int_0^t dt'[2\cos(\omega_0 t') - 1]\sin[\omega_0(t-t')]\delta\eta(t'). \tag{49}$$

We can also obtain the solutions in the Fourier domain, which would help evaluate Eq. (29):

$$\delta\tilde{x}_j(\omega) = \frac{C_j}{m\left(\omega^2 - \omega_0^2\right)}[\delta\tilde{\eta}(\omega-\omega_0) + \delta\tilde{\eta}(\omega+\omega_0) - \delta\tilde{\eta}(\omega)]. \tag{50}$$

To understand if the one-loop interferometer can be approximated as a closed loop, we also need to understand the evolution of the momentum.

$$p_j = \frac{\partial L_j}{\partial\dot{x}} = m\dot{x}_j \Rightarrow \delta p_j(t) = m\delta\dot{x}_j(t).$$

Thus, from Eq. (20), we obtain

$$p_j(t) = -\frac{C_j\eta_0}{\omega_0}\sin(\omega_0 t). \tag{51}$$

From Eq. (48), we obtain

$$\Rightarrow \delta p_j(t) = -C_j\int_0^t dt'[2\cos(\omega_0 t') - 1]\cos[\omega_0(t-t')]\,\delta\eta(t'), \tag{52}$$

where, $p_j^{\text{tot}}(t) = p_j(t) + \delta p_j(t)$. In the Fourier domain,

$$\delta\tilde{p}_j(\omega) = -\frac{i\omega C_j}{m\left(\omega^2-\omega_0^2\right)}[\delta\tilde{\eta}(\omega-\omega_0) + \delta\tilde{\eta}(\omega+\omega_0) - \delta\tilde{\eta}(\omega)]. \tag{53}$$

B. Calculating the contrast

Since we are considering a harmonic oscillator case, we will compute the expected contrast loss for the ground-state wave function, a Gaussian:

$$\psi = \left(\frac{1}{2\pi\sigma_0^2}\right)^{1/4}\exp\left(-\frac{x^2}{4\sigma_0^2}\right), \tag{54}$$

where

$$\sigma_0 \equiv \sigma_x(t=0) = \sqrt{\frac{\hbar}{2m\omega_0}}. \tag{55}$$

We consider $\hbar = 1$. Contrast is given by Refs. [46–49]:

$$\mathcal{C}(t) = \exp\left(-\frac{1}{2}\left[\left(\frac{\Delta x(t)}{\sigma_x}\right)^2 + \left(\frac{\Delta p(t)}{\sigma_p}\right)^2\right]\right), \tag{56}$$

where $\Delta x(t)$ and $\Delta p(t)$ are the differences in position and momentum between the two arms of the interferometer, at time t:

$$\Delta x(t) = x_R^{\text{tot}}(t) - x_L^{\text{tot}}(t) = \delta x_R(t) - \delta x_L(t), \tag{57}$$

$$\Delta p(t) = p_R^{\text{tot}}(t) - p_L^{\text{tot}}(t) = \delta p_R(t) - \delta p_L(t) - \frac{2\hbar\gamma_e\eta_0}{\omega_0}\sin(\omega_0 t). \tag{58}$$

Note that $\delta p \approx O(10^{-12}\delta x)$ due to the small mass of the particle, $m \approx O(10^{-15}$ kg). Hence, the dominant term contributing to Δp comes from solving the unperturbed equation of motion $\Delta p \equiv (-2\hbar\gamma_e\eta_0/\omega_0)\sin(\omega_0 t)$. Therefore, assuming minimum uncertainty, we obtain

$$\sigma_p = \frac{1}{2\sigma_x}. \tag{59}$$

In each run of the experiment, at the final evolution time $T_{\text{expt}} = 2\pi/\omega_0$, the interferometer must be closed such that the wavepackets corresponding to different spin components

overlap sufficiently in space. However, to extract the full interference pattern via spin readout, data must be accumulated over multiple experimental runs. Consequently, the theoretical estimation of contrast requires analysis at both the single-run and ensemble-averaged levels, as defined in Eq. (56). The single-run contrast depends on a specific realization of the noise, which is generally unknown and must therefore be evaluated through numerical simulation. In contrast, the ensemble-averaged contrast can be computed analytically, as it relies on the known statistical properties of the noise. The ensemble average is given by [46–49]

$$\mathcal{C}(t) = \exp\left[-\frac{1}{2}\left(\frac{\langle \Delta x(t)^2\rangle}{\sigma_x^2} + 4\sigma_x^2\langle \Delta p(t)^2\rangle\right)\right]. \tag{60}$$

Now we will compute the theoretical values of contrast expected in the case of different noise statistics: white noise and flicker noise.

Since we are interested in a one-loop interferometer, we take measurements at $t = T_{\text{expt}} = 2\pi/\omega_0$. The width of a Gaussian wave function after a one-loop interferometer ideally returns to the original width of the wave function, see Ref. [58]. Hence,

$$\sigma_x = \sqrt{\frac{\hbar}{2m\omega_0}}. \tag{61}$$

To evaluate the deviation in trajectory arising from noise in a single experimental run, we numerically simulate the two types of noise, white noise and flicker ($1/f$) noise, independently. The algorithm generates noise in the frequency domain by first defining the appropriate power spectral density (PSD) corresponding to each noise type. The spectral characteristics are introduced by weighting a complex Gaussian random generator with the square root of the PSD, ensuring that the generated frequency-domain signal exhibits the desired statistical properties. This noise is then used to compute the deviation in each of the trajectories (left and right arms of the interferometer) by solving the perturbed equations of motion in the Fourier domain, Eqs. (50) and (53). The resulting deviations in position and momentum are transformed to the time domain via inverse Fourier transform and are subsequently used to calculate the expected contrast. This enables an assessment of whether the noise-induced deviations in the trajectory are small enough to allow measurement at the end of the interferometer. The values of the parameters used in the algorithm are from Sec. IV A and based on the upper bounds on the source-dependent parameters obtained in the previous sections [Eq. (40) for white noise and Eq. (45) for flicker noise].

White noise and flicker noise

From Figs. 5(a) and 5(b), we observe that the contrast in the cases of white noise or flicker noise affecting the system is one. The deviations in the trajectory are extremely small [$O(10^{-19}$ m)] as compared to the size of the spatial superposition $\Delta x \approx O(10^{-9}$ m). The plots have been generated for the values of the source parameters obtained in the case of $\approx$10% coherence [Eq. (40) for white noise and Eq. (45) for flicker noise]. Hence, the ensemble averages in each of the cases, too, will be expected to have high contrast.

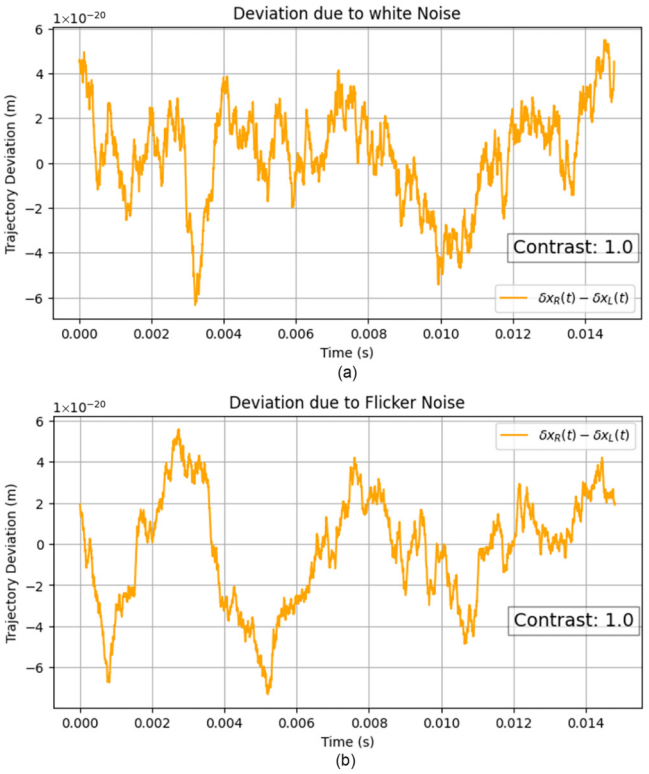

FIG. 5. Numerical simulations of trajectory deviations $\delta x_R(t) - \delta x_L(t)$ for (a) white noise and (b) flicker noise, using system parameters from Sec. IV A. The y axis is represented in terms of meters. The noise amplitudes are set according to bounds in Eqs. (40) and (45), corresponding to a dephasing rate of $\approx 10^2$ Hz, respectively. In both cases, the resulting deviations are on the order of 10^{-19} m, which is several orders of magnitude smaller than the interferometer's spatial superposition length ($\approx 10^{-9}$ m). Consequently, the contrast remains unity, indicating that noise-induced decoherence is negligible under these conditions.

The following is the explicit expression of the ensemble average of contrast in the case of white noise.

$$\begin{aligned}\langle \Delta x^2(T)\rangle &= \langle [\delta x_R(T) - \delta x_L(T)]^2\rangle \\ &= \left(\frac{2\hbar\gamma_e A}{m\omega_0}\right)^2 \frac{2\pi}{\omega_0} = 4\times 10^{-70}, \end{aligned}\tag{62}$$

$$\langle \Delta p^2(T)\rangle \approx \left\langle \left(\frac{2\hbar\gamma_e\eta_0}{\omega_0}\right)^2 \right\rangle = 5.25\times 10^{-22}. \tag{63}$$

Thus, $\mathcal{C}(T) \approx 1$. This indicates that the noise in a magnetic field can be controlled such that the loss in contrast is negligible. The integral in the case of the flicker noise is more complex, involving trigonometric integrals. However, analytical approximations in both the low- and high-frequency regimes yield results of comparable magnitude to Eq. (63). Thus, we conclude that loss of contrast due to Gaussian noise in current fluctuations bounded by values corresponding to a dephasing rate of 10^2 Hz is negligible.

VI. CONCLUSIONS

In this work, we have analyzed the impact of magnetic-field-gradient noise on the phase evolution of a quantum system modeled as a harmonic oscillator in an interferometric setup. By introducing noise at the Lagrangian level as a stochastic perturbation, we derived analytic expressions for the phase noise variance under two distinct spectral regimes: Gaussian white noise and flicker noise ($1/f$ noise), both of which are relevant to real-world experimental environments. We provide a general expression for the effective transfer function of a harmonic oscillator subject to noise, which can be readily adapted to other physical systems with similar dynamics.

We established practical constraints on the noise amplitude for both noise types. For white noise, the gradient noise amplitude must satisfy $A \leqslant 2.9 \times 10^{-6}\ \mathrm{T\,m^{-1}\,Hz^{-1/2}}$, which corresponds to a maximum allowable current noise-to-signal ratio of $\delta I/I \leqslant 1.3 \times 10^{-8}$. Similarly, for flicker noise, the source-dependent term was determined to be $K \leqslant 0.7 \times 10^{-13}\ \mathrm{T\,m^{-1}\,A^{-1}}$, leading to a comparable constraint of $\delta I/I \leqslant 1.3 \times 10^{-8}$. These limits were derived using analytical and numerical methods, for system parameters such as the effective harmonic frequency ω_0 derived following models for the Stern-Gerlach-type setup [53,54].

Thus, our theoretical analysis revealed that white noise leads to a higher dephasing rate compared to flicker noise. Nevertheless, both types of noise were found to impose nearly identical upper bounds on the permissible noise-to-signal ratio in the current source for a tolerable dephasing rate of approximately $\Gamma \approx 10^2$ Hz. This observation suggests that the experimental tolerance to current fluctuations is largely insensitive to the exact spectral character of the noise within a physically relevant range of the spectral exponent $\alpha \in [0, 1.5]$. Such robustness provides a valuable degree of flexibility in experimental design and noise mitigation strategies.

Next, we turned to the Humpty-Dumpty problem of the fluctuations causing deviations in the trajectory such that the interferometer may not close. We developed a numerical simulation framework that generates synthetic noise in the frequency domain to compute the contrast of the interferometer output for a single run of the experiment.

The simulation results confirm that the trajectory deviations are several orders of magnitude smaller than the characteristic experimental superposition length scale (i.e., $\approx 10^{-19}$ m compared to $\approx 10^{-9}$ m). Consequently, the resulting contrast remains close to unity in both noise scenarios, indicating that the Humpty-Dumpty problem is negligible and that meaningful measurements can be conducted. Our findings deliver a theoretical and computational framework for assessing the effects of noise in magnetic-field gradients in Stern-Gerlach-type interferometry.

ACKNOWLEDGMENTS

A.G. is supported in part by NSF Grants No. PHY-2110524 and No. PHY-2111544, the Heising-Simons Foundation, the W. M. Keck Foundation, the John Templeton Foundation, DARPA, and ONR Grant No. N00014-18-1-2370. S.B.'s work is supported by the EPSRC Grant No. EP/Y004590/1 MACON-QC. A.G., S.B., and A.M.'s research is funded by the Gordon and Betty Moore Foundation through Grant No. GBMF12328, DOI 10.37807/GBMF12328. This material is based on work supported by the Alfred P. Sloan Foundation under Grant No. G-2023-21130. S.N.M. would like to thank the organizers of the workshop, Schrodinger Cats: The quest to find the edge of the quantum world, held at OIST, Japan for facilitating academic interactions that led to this collaboration. S.N.M. acknowledges support from the Kishore Vaigyanik Protsahan Yojana (KVPY) fellowship, SX-2011055, awarded by the Department of Science and Technology, Government of India. S.B. would like to acknowledge EPSRC Grants No. EP/N031105/1, No. EP/S000267/1, and No. EP/X009467/1 and STFC Grant No. ST/W006227/1.

DATA AVAILABILITY

The data that support the findings of this article are openly available [82].

APPENDIX A: DERIVATION OF GENERAL FORM OF THE DEPHASING RATE

In this section, we derive the general form of the dephasing rate from the variation in the Lagrangian of a system due to noise. We ignore deviations in the trajectory. However, the method can be extrapolated to the same. We start by expressing the explicit time-dependence of the noisy terms in Eq. (4),

$$(\delta\phi\delta\phi^*) = \frac{1}{\hbar^2}\int_{t_i}^{t_f}\int_{t_i}^{t_f} \Big|\Big\{\big[\delta A_R(t)x_R^2 - \delta A_L(t)x_L^2\big] + [\delta B_R(t)x_R - \delta B_L(t)x_L] + [\delta C_R(t) - \delta C_L(t)]\Big\}dt\Big|^2. \tag{A1}$$

Generally, we know the statistics of the noise as a function of the frequency of the noise. Hence, we take a Fourier transform of the time-dependent coefficients:

$$(\delta\phi\delta\phi^*) = \frac{1}{\hbar^2}\left|\int_{t_i}^{t_f}\int_{\omega_{\min}}^{\infty}\big[\big(\delta\tilde{A}_R(\omega)x_R^2 - \delta\tilde{A}_L(\omega)x_L^2\big) + (\delta\tilde{B}_R(\omega)x_R - \delta\tilde{B}_L(\omega)x_L) + (\delta\tilde{C}_R(\omega) - \delta\tilde{C}_L(\omega))\big]e^{i\omega t}\,d\omega\,dt\right|^2. \tag{A2}$$

Now, we invoke the assumption that δA_L and δB_L are some linear functions in δA_R and δB_R, respectively. Let

$$\delta A_j(t) = S_{xj}D_{As}f_{As}(t) + D_{An}f_{An}(t), \tag{A3}$$

$$\delta B_j(t) = S_{xj}D_{Bs}f_{Bs}(t) + D_{Bn}f_{Bn}(t), \tag{A4}$$

$$\delta C_j(t) = D_{Cj}f_{Cj}(t), \tag{A5}$$

where D_{An} is the coefficient of the spin-independent part of δA_j that is dependent on noise:

$$\begin{aligned}\delta\phi\delta\phi^* = \frac{1}{\hbar^2}\Bigg| \int_{t_i}^{t_f}\int_{\omega_{\min}}^{\infty} \big[\tilde{f}_{An}(\omega)D_{An}\big(x_R^2 - x_L^2\big) \\ + \tilde{f}_{As}(\omega)D_{As}\big(x_R^2 + x_L^2\big) + \tilde{f}_{Bn}(\omega)D_{Bn}(x_R - x_L) \\ + \tilde{f}_{Bs}(\omega)D_{Bs}(x_R + x_L) + D_{CR}\tilde{f}_{CR}(\omega) \\ - D_{CL}\tilde{f}_{CL}(\omega)\big]e^{i\omega t}\, d\omega\, dt\Bigg|^2. \end{aligned} \tag{A6}$$

Now consider a single source of noise. Hence,

$$f_{As}(t) = f_{An}(t) = f_{Bs}(t) = f_{Bn}(t) = f_{Cj}(t) = f(t). \tag{A7}$$

Hence,

$$\begin{aligned}\delta\phi\delta\phi^* &= \frac{1}{\hbar^2}\Bigg| \int_{t_i}^{t_f}\int_{\omega_{\min}}^{\infty} \tilde{f}(\omega)\big[D_{An}\big(x_R^2 - x_L^2\big) + D_{As}\big(x_R^2 + x_L^2\big) \\ &\quad + D_{Bn}(x_R - x_L) + D_{Bs}(x_R + x_L) \\ &\quad + (D_{CR} - D_{CL})\big]e^{i\omega t} d\omega dt\Bigg|^2 \qquad \text{(A8)} \\ &= \frac{1}{\hbar^2}\int_{\omega_{\min}}^{\infty}\int_{\omega_{\min}}^{\infty} \tilde{f}(\omega)\tilde{f}(\omega') \\ &\quad \times \Bigg| \int_{t_i}^{t_f} \big[D_{An}\big(x_R^2 - x_L^2\big) + D_{As}\big(x_R^2 + x_L^2\big) \\ &\quad + D_{Bn}(x_R - x_L) + D_{Bs}(x_R + x_L) \\ &\quad + (D_{CR} - D_{CL})\big]e^{i\frac{(\omega+\omega')}{2}t} dt\Bigg|^2 d\omega d\omega'. \qquad \text{(A9)}\end{aligned}$$

Ultimately, what concerns us is the variance of the phase difference due to noise:

$$\begin{aligned}E[\delta\phi\delta\phi^*] = \frac{1}{\hbar^2}\int_{\omega_{\min}}^{\infty}\int_{\omega_{\min}}^{\infty} E[\tilde{f}(\omega)\tilde{f}(\omega')] \\ \times \Bigg| \int_{t_i}^{t_f} \big[D_{An}\big(x_R^2 - x_L^2\big) + D_{As}\big(x_R^2 + x_L^2\big) \\ + D_{Bn}(x_R - x_L) + D_{Bs}(x_R + x_L) \\ + (D_{CR} - D_{CL})\big]e^{i\frac{(\omega+\omega')}{2}t} dt\Bigg|^2 d\omega d\omega'. \end{aligned} \tag{A10}$$

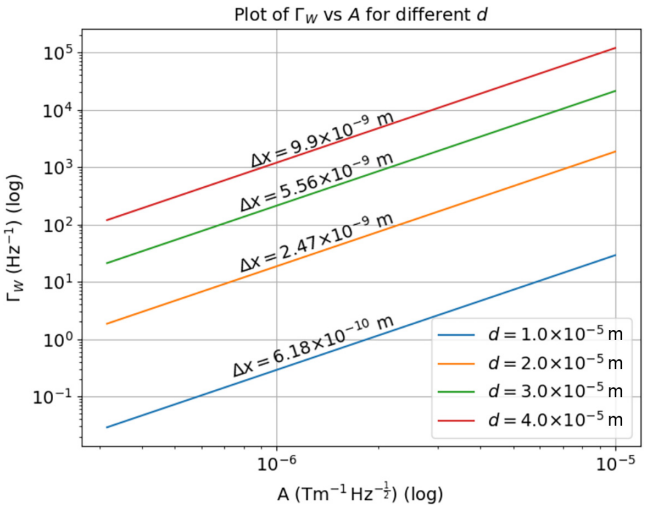

FIG. 6. Log-log plot of Γ_W versus A for various values of the separation distance d. The data exhibit a clear linear trend, indicating a power-law relationship. Each curve corresponds to a different distance d of the particle from the wire, with associated maximum superposition distance being Δx labeled. The slope remains consistent across curves, while the intercept varies with d, highlighting its influence on noise sensitivity. This is the log-log plot of Fig. 1.

Thus, from Eq. (5), we obtain

$$\begin{aligned}\Gamma = \frac{1}{\hbar^2}\int_{\omega_{\min}}^{\infty} S(\omega)\Bigg| \int_{t_i}^{t_f} \big[D_{An}\big(x_R^2 - x_L^2\big) + D_{As}\big(x_R^2 + x_L^2\big) \\ + D_{Bn}(x_R - x_L) + D_{Bs}(x_R + x_L) \\ + (D_{CR} - D_{CL})\big]e^{i\omega t} dt\Bigg|^2 d\omega \qquad \text{(A11)} \\ = \frac{1}{\hbar^2}\int_{\omega_{\min}}^{\infty} S(\omega)|\Sigma_i\sqrt{F_i(\omega)}|^2 d\omega, \qquad \text{(A12)}\end{aligned}$$

where $F_1(\omega) = |\int_{t_i}^{t_f} dt\, D_{An}(x_R - x_L)e^{i\omega t}|^2$.

APPENDIX B: ANALYTICAL EXPRESSION FOR DEPHASING RATE IN THE CASE OF WHITE NOISE

In Fig. 6, we observe that the log-log plot of Γ_W vs A follows a linear trend. Fitting the graphs, we obtain

$$\log(\Gamma_W) \approx 2\log(A) + c_W(d), \tag{B1}$$

where $c_W(d)$ is the y intercept as a function of d. We obtain the following relation for $c_W(d)$ via graphical analysis:

$$c_W(d) \approx 6\log(d) + 41.4680. \tag{B2}$$

For $d = 2\times10^{-5}$ m to a linear curve, we obtain

$$\begin{aligned}\log(\Gamma_W) &\approx 2\log(A) + 13.274 \\ \Rightarrow \Gamma_W &\approx 1.88A^2\times10^{13}. \end{aligned} \tag{B3}$$

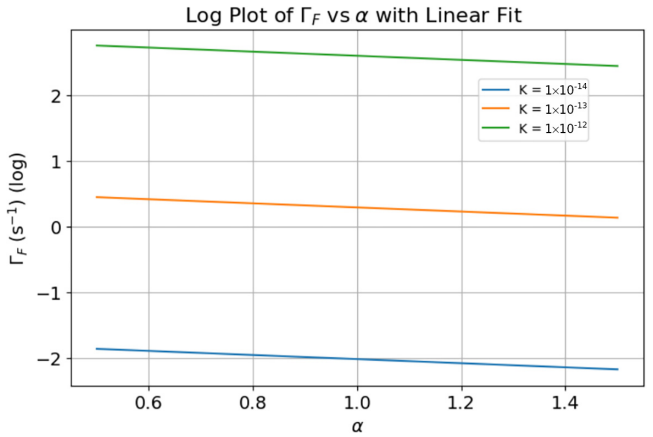

FIG. 7. Plot of Γ_F versus spectral exponent α for noise strengths $K = 10^{-14}, 10^{-13}, 10^{-12}$ in the case of flicker ($1/f$) noise. While the main analysis in the paper focuses on $\alpha = 1$, this plot demonstrates that the dephasing rate Γ_F remains within the same order of magnitude across a range of α values for each fixed K. This supports the validity of extrapolating the constraints derived at $\alpha = 1$ to systems characterized by other values of α.

APPENDIX C: ANALYTICAL EXPRESSION FOR DEPHASING RATE IN THE CASE OF FLICKER NOISE

Linear fitting of the graphs in Fig. 3 yields

$$\log(\Gamma_F) \approx \log(K) + c_F(d), \tag{C1}$$

where $c_F(d)$ is the y intercept as a function of d. We obtain the following relation for $c_F(d)$ via graphical analysis:

$$c_F(d) \approx 6\log(d) + 43.5567. \tag{C2}$$

Thus, corresponding to $d = 20$ μm we obtain

$$\log(\Gamma_F) \approx \log(K) + 15.3629$$
$$\Rightarrow \Gamma_F \approx 2.31K \times 10^{15}. \tag{C3}$$

To assess the robustness of our results with respect to variations in the spectral exponent α, we compute the dephasing rate Γ_F as a function of α for different values of the noise strength K. While our primary analysis focuses on the case $\alpha = 1$, corresponding to $1/f$ noise, the results shown in Fig. 7, demonstrate that Γ_F remains within the same order of magnitude across a range of α values for each fixed K. This indicates that the scaling of the dephasing rate is not highly sensitive to the precise value of α, thereby justifying the extension of our constraints on $\delta I/I$ to materials or environments where $\alpha \neq 1$.

APPENDIX D: DEPHASING RATE ON INCLUSION OF THE DEVIATION IN TRAJECTORY DUE TO NOISE

On substituting for deviations in the trajectory [Eq. (50)] in Eq. (25), we obtain the total phase difference between the two arms of the interferometer due to noise:

$$\delta\phi = H\left(\int_{-\infty}^{-\omega_{\min}} + \int_{\omega_{\min}}^{\infty}\right)\left[\delta\tilde{\eta}(\omega)\int_0^T\left\{\frac{\cos(\omega_0 t)[\cos(\omega_0 t)-1]}{\omega_0^2} + \frac{[2\cos(\omega_0 t)-1]\cos(\omega_0 t)}{(\omega^2-\omega_0^2)}\right\}e^{i\omega t}dt\right]d\omega. \tag{D1}$$

TABLE II. Order-of-magnitude values used in estimating dephasing contributions. The values of x_j, η_0 and $\frac{\delta I}{I}$ are consistent with values used throughout the paper. The value of δx_j is obtained from numerical simulations similar to those in Sec. V.

Quantity	Value
Typical position, x_j	10^{-9} m
Magnetic field gradient, η_0	6×10^3 T/m
Trajectory deviation, δx_j	10^{-15} m
Gradient fluctuation, $\delta\eta = \frac{\delta I}{I}\eta_0$	6×10^{-5} T/m

Dephasing rate accounting for terms arising only from deviations in the trajectory arises from the second term in Eq. (D1). This is given by

$$\Gamma_{\text{dev}} = \frac{8H^2}{\omega_0^5}\int_1^\infty S(\xi)F_{\text{dev}}(\xi)d\xi, \tag{D2}$$

where $\xi = \omega/\omega_0$:

$$F_{\text{dev}}(\xi) = \frac{\sin^2(\pi\xi)}{(1-\xi^2)^2}\left[\frac{1}{\xi} - \frac{\xi}{\xi^2-1} + \frac{\xi}{\xi^2-4}\right]^2. \tag{D3}$$

Thus, from Eq. (6), we obtain the following to be the additional contribution to the dephasing rate:

$$\Gamma_{tot} = \frac{8H^2}{\omega_0^5}\int_1^\infty S(\xi)(\sqrt{F_{\text{HO}}(\xi)} + \sqrt{F_{\text{dev}}(\xi)})^2 d\xi. \tag{D4}$$

We perform an order-of-magnitude estimate using parameter values drawn from Secs. IV A and V to verify that the dephasing rate due to trajectory deviations, denoted Γ_{dev}, does not exceed the order of magnitude of the dephasing rate calculated without accounting for such deviations [i.e., Eq. (29)]. This estimation is carried out using values in Table II.

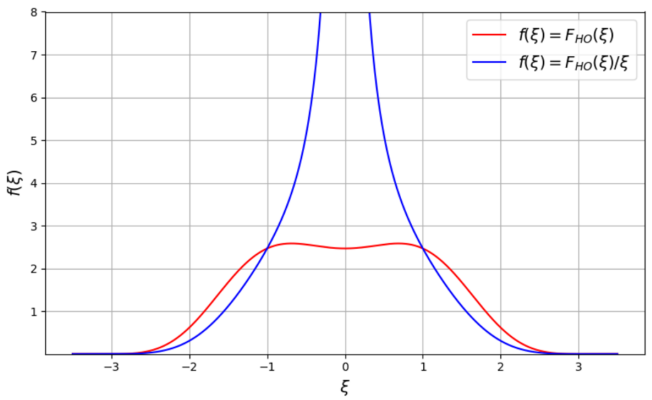

FIG. 8. The graph shows the nature of the integrands in Eq. (29) as a function of $\xi = \omega/\omega_0$ in case of white noise (red curve) and flicker noise (blue curve). Nature of integrands used to compute the dephasing. It exhibits how, for $\xi > 1$, the area under the curve in the case of flicker noise is less than that of white noise. We observe how the seeming singularities in Eq. (30) at $\xi = 1, 2$ are removable singularities. It also helps visualize how the dephasing in the case of white noise, which has equal strength across the frequency spectrum, gives rise to finite dephasing as a result of the system not being susceptible to higher frequencies of noise.

Using these values, we estimate the two types of contributions to the dephasing in Eq. (25), one involving the fluctuations directly in the magnetic field gradient and the other involving the fluctuations in the trajectory as a result of fluctuations in the field gradient. We note from Eq. (25) that the dephasing is proportional to $x_j\delta\eta$ and $\delta x_j\eta_0$. Hence, we use these values to estimate the order of magnitude of the two types of contributions to the dephasing:

$$x_j\delta\eta \approx 10^{-13}\ \mathrm{T}, \tag{D5}$$

$$\delta x_j\eta_0 \approx 10^{-11}\ \mathrm{T}. \tag{D6}$$

These contributions suggest that the dephasing due to deviations cannot be neglected. Hence, we have to explicitly account for the contribution of the deviations in the trajectory to the dephasing.

From the above analysis, we also note that, although the deviations in trajectory may be small enough to close the interferometer, i.e., we can have contrast = 1, the deviations in the trajectory contribute to the dephasing and have to be accounted for while obtaining precise bounds on experimental parameters.

APPENDIX E: NATURE OF THE TRANSFER FUNCTION AND PSD

To gain insight into how different noise spectra contribute to dephasing, we examine the behavior of the integrand in Eq. (29), plotted in Fig. 8 as a function of the normalized frequency $\xi = \omega/\omega_0$. The red curve corresponds to white noise, characterized by a flat spectral density, while the blue curve represents flicker noise, where the spectral density scales as $1/\omega$. For $\xi > 1$, the integrand associated with flicker noise lies below that of white noise, reflecting the fact that flicker noise is predominantly concentrated at low frequencies. Despite the constant strength of white noise across the spectrum, the system's frequency response $F_{\mathrm{HO}}(\omega)$ suppresses contributions from higher frequencies, ensuring that the dephasing rate remains finite. The figure also highlights that the apparent singularities in the harmonic oscillator response function at $\xi = 1$ and $\xi = 2$, as suggested by Eq. (30), are in fact removable and do not lead to divergences. These highlight how the interplay between the noise spectrum and the system's susceptibility determines the extent of dephasing, and they help justify the convergence properties of the integral in both the white and flicker noise cases.

[1] M. W. Doherty, N. B. Manson, P. Delaney, F. Jelezko, J. Wrachtrup, and L. C. Hollenberg, The nitrogen-vacancy colour centre in diamond, Phys. Rep. **528**, 1 (2013).

[2] S. Bose, A. Mazumdar, G. W. Morley, H. Ulbricht, M. Toroš, M. Paternostro, A. A. Geraci, P. F. Barker, M. S. Kim, and G. Milburn, Spin entanglement witness for quantum gravity, Phys. Rev. Lett. **119**, 240401 (2017).

[3] https://www.youtube.com/watch?v = 0Fv-0k13s_k (2016), accessed 1/11/22.

[4] R. J. Marshman, A. Mazumdar, and S. Bose, Locality and entanglement in table-top testing of the quantum nature of linearized gravity, Phys. Rev. A **101**, 052110 (2020).

[5] S. Bose, A. Mazumdar, M. Schut, and M. Toroš, Mechanism for the quantum natured gravitons to entangle masses, Phys. Rev. D **105**, 106028 (2022).

[6] C. Marletto and V. Vedral, Gravitationally-induced entanglement between two massive particles is sufficient evidence of quantum effects in gravity, Phys. Rev. Lett. **119**, 240402 (2017).

[7] D. L. Danielson, G. Satishchandran, and R. M. Wald, Gravitationally mediated entanglement: Newtonian field versus gravitons, Phys. Rev. D **105**, 086001 (2022).

[8] D. Carney, P. C. E. Stamp, and J. M. Taylor, Tabletop experiments for quantum gravity: a user's manual, Class. Quantum Grav. **36**, 034001 (2019).

[9] D. Carney, K. G. Leach, and D. C. Moore, Searches for massive neutrinos with mechanical quantum sensors, PRX Quantum **4**, 010315 (2023).

[10] D. Biswas, S. Bose, A. Mazumdar, and M. Toroš, Gravitational optomechanics: Photon-matter entanglement via graviton exchange, Phys. Rev. D **108**, 064023 (2023).

[11] M. Christodoulou, A. Di Biagio, M. Aspelmeyer, Č. Brukner, C. Rovelli, and R. Howl, Locally mediated entanglement in linearized quantum gravity, Phys. Rev. Lett. **130**, 100202 (2023).

[12] M. Christodoulou and C. Rovelli, On the possibility of laboratory evidence for quantum superposition of geometries, Phys. Lett. B **792**, 64 (2019).

[13] P. G. C. Rufo, A. Mazumdar, and C. Sabín, Genuine tripartite entanglement in graviton-matter interactions, Phys. Rev. A **111**, 022444 (2025).

[14] F. Hanif, D. Das, J. Halliwell, D. Home, A. Mazumdar, H. Ulbricht, and S. Bose, Testing whether gravity acts as a quantum entity when measured, Phys. Rev. Lett. **133**, 180201 (2024).

[15] R. Horodecki, P. Horodecki, M. Horodecki, and K. Horodecki, Quantum entanglement, Rev. Mod. Phys. **81**, 865 (2009).

[16] M. Toroš, M. Schut, P. Andriolo, S. Bose, and A. Mazumdar, Relativistic dips in entangling power of gravity, Phys. Rev. D **111**, 036026 (2025).

[17] M. Toroš, P. Andriolo, M. Schut, S. Bose, and A. Mazumdar, Relativistic effects on entangled single-electron traps, Phys. Rev. D **110**, 056031 (2024).

[18] S. G. Elahi and A. Mazumdar, Probing massless and massive gravitons via entanglement in a warped extra dimension, Phys. Rev. D **108**, 035018 (2023).

[19] U. K. Beckering Vinckers, Á. de la Cruz-Dombriz, and A. Mazumdar, Quantum entanglement of masses with nonlocal gravitational interaction, Phys. Rev. D **107**, 124036 (2023).

[20] S. Chakraborty, A. Mazumdar, and R. Pradhan, Distinguishing Jordan and Einstein frames in gravity through entanglement, Phys. Rev. D **108**, L121505 (2023).

[21] P. F. Barker, S. Bose, R. J. Marshman, and A. Mazumdar, Entanglement based tomography to probe new macroscopic forces, Phys. Rev. D **106**, L041901 (2022).

[22] S. Bose, A. Mazumdar, M. Schut, and M. Toroš, Entanglement witness for the weak equivalence principle, Entropy **25**, 448 (2023).

[23] M.-Z. Wu, M. Toroš, S. Bose, and A. Mazumdar, Quantum gravitational sensor for space debris, Phys. Rev. D **107**, 104053 (2023).

[24] M.-Z. Wu, M. Toroš, S. Bose, and A. Mazumdar, Inertial torsion noise in matter-wave interferometers for gravity experiments, Phys. Rev. D **111**, 064004 (2025).

[25] M. Toroš, T. W. van de Kamp, R. J. Marshman, M. S. Kim, A. Mazumdar, and S. Bose, Relative acceleration noise mitigation for nanocrystal matter-wave interferometry: Applications to entangling masses via quantum gravity, Phys. Rev. Res. **3**, 023178 (2021).

[26] M. Schut, H. Bosma, M.-Z. Wu, M. Toroš, S. Bose, and A. Mazumdar, Dephasing due to electromagnetic interactions in spatial qubits, Phys. Rev. A **110**, 022412 (2024).

[27] P. Fragolino, M. Schut, M. Toroš, S. Bose, and A. Mazumdar, Decoherence of a matter-wave interferometer due to dipole-dipole interactions, Phys. Rev. A **109**, 033301 (2024).

[28] R. Zhang, M. Schut, and A. Mazumdar, Vacuum fluctuations induced decoherence of a diamagnetic nanosphere, arXiv:2501.07632.

[29] K. Sinha and P. W. Milonni, Dipoles in blackbody radiation: momentum fluctuations, decoherence, and drag force, J. Phys. B **55**, 204002 (2022).

[30] T. Zhou, R. Rizaldy, M. Schut, and A. Mazumdar, Spin contrast, finite temperature, and noise in matter-wave interferometer, arXiv:2503.13656.

[31] R. J. Marshman, A. Mazumdar, G. W. Morley, P. F. Barker, S. Hoekstra, and S. Bose, Mesoscopic interference for metric and curvature (MIMAC) & gravitational wave detection, New J. Phys. **22**, 083012 (2020).

[32] A. Bassi, K. Lochan, S. Satin, T. P. Singh, and H. Ulbricht, Models of wave-function collapse, underlying theories, and experimental tests, Rev. Mod. Phys. **85**, 471 (2013).

[33] S. Rijavec, M. Carlesso, A. Bassi, V. Vedral, and C. Marletto, Decoherence effects in non-classicality tests of gravity, New J. Phys. **23**, 043040 (2021).

[34] T. W. van de Kamp, R. J. Marshman, S. Bose, and A. Mazumdar, Quantum gravity witness via entanglement of masses: Casimir screening, Phys. Rev. A **102**, 062807 (2020).

[35] M. Schut, J. Tilly, R. J. Marshman, S. Bose, and A. Mazumdar, Improving resilience of quantum-gravity-induced entanglement of masses to decoherence using three superpositions, Phys. Rev. A **105**, 032411 (2022).

[36] M. Schut, A. Grinin, A. Dana, S. Bose, A. Geraci, and A. Mazumdar, Relaxation of experimental parameters in a quantum-gravity-induced entanglement of masses protocol using electromagnetic screening, Phys. Rev. Res. **5**, 043170 (2023).

[37] M. Schut, A. Geraci, S. Bose, and A. Mazumdar, Micrometer-size spatial superpositions for the QGEM protocol via screening and trapping, Phys. Rev. Res. **6**, 013199 (2024).

[38] M. Schut, P. Andriolo, M. Toroš, S. Bose, and A. Mazumdar, Expression for the decoherence rate due to air-molecule scattering in spatial qubits, Phys. Rev. A **111**, 042211 (2025).

[39] C. Henkel and R. Folman, Internal decoherence in nano-object interferometry due to phonons, AVS Quantum Sci. **4**, 025602 (2022).

[40] C. Henkel and R. Folman, Universal limit on spatial quantum superpositions with massive objects due to phonons, Phys. Rev. A **110**, 042221 (2024).

[41] Q. Xiang, R. Zhou, S. Bose, and A. Mazumdar, Phonon induced contrast in matter wave interferometer, Phys. Rev. A **110**, 042614 (2024).

[42] Y. Japha and R. Folman, Quantum uncertainty limit for Stern-Gerlach interferometry with massive objects, Phys. Rev. Lett. **130**, 113602 (2023).

[43] T. Zhou, S. Bose, and A. Mazumdar, Gyroscopic stability for nanoparticles in Stern-Gerlach interferometry and spin contrast, arXiv:2407.15813.

[44] O. Romero-Isart, Quantum superposition of massive objects and collapse models, Phys. Rev. A **84**, 052121 (2011).

[45] K. Hornberger, S. Gerlich, P. Haslinger, S. Nimmrichter, and M. Arndt, *Colloquium*: Quantum interference of clusters and molecules, Rev. Mod. Phys. **84**, 157 (2012).

[46] B. Englert, J. Schwinger, and M. O. Scully, Is spin coherence like Humpty-Dumpty? I. Simplified treatment, Found. Phys. **18**, 1045 (1988).

[47] J. Schwinger, M. O. Scully, and B. G. Englert, Is spin coherence like Humpty-Dumpty? Z. Phys. D **10**, 135 (1988).

[48] M. O. Scully, B.-G. Englert, and J. Schwinger, Spin coherence and Humpty-Dumpty. III. The effects of observation, Phys. Rev. A **40**, 1775 (1989).

[49] Y. Margalit, O. Dobkowski, Z. Zhou, O. Amit, Y. Japha, S. Moukouri, D. Rohrlich, A. Mazumdar, S. Bose, C. Henkel, and R. Folman, Realization of a complete Stern-Gerlach interferometer: Towards a test of quantum gravity, Sci. Adv. **7**, eabg2879 (2021).

[50] O. Amit, Y. Margalit, O. Dobkowski, Z. Zhou, Y. Japha, M. Zimmermann, M. A. Efremov, F. A. Narducci, E. M. Rasel, W. P. Schleich *et al.*, T^3 Stern-Gerlach matter-wave interferometer, Phys. Rev. Lett. **123**, 083601 (2019).

[51] C. Wan, M. Scala, G. W. Morley, ATM. A. Rahman, H. Ulbricht, J. Bateman, P. F. Barker, S. Bose, and M. S. Kim, Free nano-object Ramsey interferometry for large quantum superpositions, Phys. Rev. Lett. **117**, 143003 (2016).

[52] M. Scala, M. S. Kim, G. W. Morley, P. F. Barker, and S. Bose, Matter-wave interferometry of a levitated thermal nano-oscillator induced and probed by a spin, Phys. Rev. Lett. **111**, 180403 (2013).

[53] J. S. Pedernales, G. W. Morley, and M. B. Plenio, Motional dynamical decoupling for interferometry with macroscopic particles, Phys. Rev. Lett. **125**, 023602 (2020).

[54] R. J. Marshman, A. Mazumdar, R. Folman, and S. Bose, Constructing nano-object quantum superpositions with a Stern-Gerlach interferometer, Phys. Rev. Res. **4**, 023087 (2022).

[55] R. Zhou, R. J. Marshman, S. Bose, and A. Mazumdar, Gravito-diamagnetic forces for mass independent large spatial quantum superpositions, Phys. Scr. **99**, 055114 (2024).

[56] R. Zhou, R. J. Marshman, S. Bose, and A. Mazumdar, Catapulting towards massive and large spatial quantum superposition, Phys. Rev. Res. **4**, 043157 (2022).

[57] R. Zhou, R. J. Marshman, S. Bose, and A. Mazumdar, Mass-independent scheme for enhancing spatial quantum superpositions, Phys. Rev. A **107**, 032212 (2023).

[58] R. Zhou, Q. Xiang, and A. Mazumdar, Spin-dependent force and inverted harmonic potential for rapid creation of macroscopic quantum superpositions, arXiv:2408.11909.

[59] L. Braccini, A. Serafini, and S. Bose, Exponential expansion of massive Schrödinger cats for sensing and entanglement, arXiv:2408.11930.

[60] R. Rizaldy, T. Zhou, S. Bose, and A. Mazumdar, Rotational stability in nanorotor and spin contrast in one-loop interferometry in the Stern-Gerlach setup, arXiv:2412.15335.

[61] Y. Japha, Unified model of matter-wave-packet evolution and application to spatial coherence of atom interferometers, Phys. Rev. A **104**, 053310 (2021).

[62] U. Delić, M. Reisenbauer, K. Dare, D. Grass, V. Vuletić, N. Kiesel, and M. Aspelmeyer, Cooling of a levitated nanoparticle to the motional quantum ground state, Science **367**, 892 (2020).

[63] J. Piotrowski, D. Windey, J. Vijayan, C. Gonzalez-Ballestero, A. de los Ríos Sommer, N. Meyer, R. Quidant, O. Romero-Isart, R. Reimann, and L. Novotny, Simultaneous ground-state cooling of two mechanical modes of a levitated nanoparticle, Nat. Phys. **19**, 1009 (2023).

[64] M. Kamba, R. Shimizu, and K. Aikawa, Nanoscale feedback control of six degrees of freedom of a near-sphere, Nat. Commun. **14**, 7943 (2023).

[65] D. S. Bykov, L. Dania, F. Goschin, and T. E. Northup, 3D sympathetic cooling and detection of levitated nanoparticles, Optica **10**, 438 (2023).

[66] M. Perdriat, C. C. Rusconi, T. Delord, P. Huillery, C. Pellet-Mary, A. Durand, B. A. Stickler, and G. Hétet, Rotational locking of charged microparticles in quadrupole ion traps, Phys. Rev. Lett. **133**, 253602 (2024).

[67] S. G. Elahi, M. Schut, A. Dana, A. Grinin, S. Bose, A. Mazumdar, and A. Geraci, Diamagnetic micro-chip traps for levitated nanoparticle entanglement experiments, arXiv:2411.02325.

[68] A. Khintchine, Korrelationstheorie der stationären stochastischen Prozesse, Math. Ann. **109**, 604 (1934).

[69] N. Wiener, Generalized harmonic analysis, Acta Math. **55**, 117 (1930).

[70] S. Sendelbach, Investigations of 1/f flux noise in superconducting quantum circuits, Ph.D. thesis, University of Wisconsin, Madison, 2013.

[71] S. A. Sergeenkov, Flicker-noise spectrum in weak-links-containing superconductors, arXiv:cond-mat/9905363.

[72] S. P. Kelly and Y. Tserkovnyak, Superconductivity-enhanced magnetic field noise, arXiv:2412.05465.

[73] J. H. Scofield, J. V. Mantese, and W. W. Webb, 1/*f* noise of metals: A case for extrinsic origin, Phys. Rev. B **32**, 736 (1985).

[74] P. Dutta and P. M. Horn, Low-frequency fluctuations in solids: $\frac{1}{f}$ noise, Rev. Mod. Phys. **53**, 497 (1981).

[75] R. Folman, P. Kruger, J. Schmiedmayer, J. Denschlag, and C. Henkel, Microscopic atom optics: From wires to an atom chip, Adv. At. Mol. Opt. Phys. **48**, 263 (2022).

[76] R. J. Marshman, S. Bose, A. Geraci, and A. Mazumdar, Entanglement of magnetically levitated massive Schrödinger cat states by induced dipole interaction, Phys. Rev. A **109**, L030401 (2024).

[77] A. Gruber, A. Dräbenstedt, C. Tietz, L. Fleury, J. Wrachtrup, and C. von Borczyskowski, Scanning confocal optical microscopy and magnetic resonance on single defect centers, Science **276**, 2012 (1997).

[78] P. W. Bowen and J. G. Milburn, *Quantum Optomechanics* (CRC Press, Boca Raton, 2015).

[79] G. Afek, F. Monteiro, B. Siegel, J. Wang, S. Dickson, J. Recoaro, M. Watts, and D. C. Moore, Control and measurement of electric dipole moments in levitated optomechanics, Phys. Rev. A **104**, 053512 (2021).

[80] J. L. Garrett, J. Kim, and J. N. Munday, Measuring the effect of electrostatic patch potentials in Casimir force experiments, Phys. Rev. Res. **2**, 023355 (2020).

[81] F. C. Wellstood, C. Urbina, and J. Clarke, Flicker (1/*f*) noise in the critical current of Josephson junctions at 0.09–4.2 K, Appl. Phys. Lett. **85**, 5296 (2004).

[82] https://github.com/SciPhyl-Sneha/Magnetic-noise-in-macroscopic-quantum-spatial-superposition.